Modelling Subaqueous and Subaerial Muddy Debris Flows

Xuesheng Qian, S.M.ASCE[1] and Himangshu S. Das, M.ASCE[2]

Abstract: Debris flows are notorious geohazards existing in both subaerial and subaqueous environments. They may cause catastrophic destructions to adjacent life and properties along their overriding path. As such, predictions of their movement are critical to future geohazard mitigations, and there is a need to develop an effective numerical model to achieve this purpose. In this paper, a two-dimensional depth-averaged numerical model is presented to simulate the movement of subaqueous and subaerial muddy debris flows. The Herschel-Bulkley rheological model is used to describe the rheology of debris flow. The conservation equations of mass and momentum in conservative forms are numerically solved using an explicit finite difference scheme. The model is applied to a series of one-dimensional laboratory experiments in subaerial environments. The model is also applied to a field

[1] Ph.D. Student, Dept. of Civil and Environmental Engineering, Jackson State Univ., Jackson, MS 39217, USA. E-mail: xsq621@gmail.com

[2] Hydraulics&Hydrology Expert, U.S. Army Corps of Engineers, Galveston, TX 77550, USA (corresponding author). E-mail: h_shekhar@hotmail.com

setting within the Na Kika Basin, Gulf of Mexico. Modelling results of deposit thickness of debris flow agree with those laboratory and field observations. Furthermore, the model is applied to two synthetic two-dimensional field conditions, one with a uniform slope and the other with a sinuous canyon. Sensitivity analyses are performed to explore the relative importance of yield stress, dynamic viscosity, bottom slope, initial failure height, and initial failure shape for runout distances of debris flow. For the application with a sinuous canyon, two different dimensions of canyon are used to demonstrate possible deposition patterns of debris flow.

Author keywords: Subaqueous and subaerial muddy debris flows; Runout distance; laboratory and field environments; One-dimensional and two-dimensional applications; Numerical modelling.

Introduction

Debris flows are gravity-driven mass flows. They are ubiquitous geophysical phenomena, which may occur in subaerial and subaqueous environments. In mountainous areas, debris flows are commonly triggered by torrential rains (Toniolo et al. 2004). The energetic gravity flows can cause catastrophic

34 destructions to human beings as well as to their properties along the flow
35 path (Hungr 1995; McDougall and Hungr 2004). Although rarely visible to
36 human eyes, debris flows may also be generated by submarine landslides on
37 continental slopes (Masson et al. 2006; Talling 2014). Many factors lead to
38 the initiation of submarine landslides. They vary from sudden impacts of
39 earthquakes and hurricanes, to long term geological processes such as
40 oversteepening, sedimentation, and underconsolidation (Hampton and Locat
41 1996; Lee et al. 2007). Upon initiation of submarine landslides, the bulk of
42 released sediment quickly mixes up with ambient seawater and transforms
43 into submarine debris flows. Driving by their gravity, they may travel long
44 distances on very gentle continental slopes (0.5°-3.0°), and their course of
45 travel may last less than an hour to several days (Elverhøi et al. 2000;
46 Talling et al. 2007). As a result, the frontal velocities of submarine debris
47 flow vary greatly. For example, velocity of up to 7 m/s has been estimated in
48 the back analysis of six slides in the Norwegian fjords between 1930 and
49 1952 (Bjerrum 1971), and 11 m/s for the 1979 landslide off the coast of
50 French town of Nice has been reported (Canals et al. 2004). With such high
51 velocities, submarine debris flows could be a potential source for the

52 generation of hazardous tsunamis (Jiang and Le Blond 1992, 1993, 1994;
53 Fine et al. 2005; Tappin 2010). During their rapid downslope movement,
54 they may also pose potential damages to offshore infrastructures such as
55 subsea pipelines, communication cables, and offshore drilling rigs (Zakeri et
56 al. 2008; Yuan et al. 2012). As such, understanding and predicting physical
57 processes of subaqueous and subaerial debris flows are critical to the future
58 geohazard mitigations, and there is a need to develop an effective numerical
59 model for debris flows. The specific objective of current work is to develop
60 a numerical model capable of simulating debris flow movement using their
61 rheological properties as they initiate from source and then propagate
62 downstream to impact adjacent structures.

63 Based on the nature of sediments, debris flows can be categorized as
64 sandy debris flows and muddy debris flows (Rzadkiewicz et al. 1997).
65 Sandy debris flows are composed of coarse grains with low cohesion,
66 whereas muddy debris flows contain relatively high content of cohesive
67 sediments. In subaerial environments, sandy debris flows are quite common,
68 and a lot of studies have been focused on them (e.g., Iverson and Denlinger
69 2001; Denlinger and Iverson 2001). On the other hand, muddy debris flows

70 in subaqueous settings are frequently addressed in geohazard assessments of
71 offshore infrastructures (Bruschi et al. 2006). They can also be found within
72 the clay-shale basins in subaerial settings (Remaître et al. 2005). Up to now,
73 various research methods have been developed and applied to understand the
74 physical processes of subaqueous and subaerial muddy debris flows. They
75 include the field investigations, laboratory experiments, and analytical and
76 numerical models. To reveal historical events of submarine mass movement
77 preserved in the sedimentary strata, a series of field investigations have been
78 carried out. One is the Strata Formation on Margins (STRATAFORM)
79 program initiated by the US Office of Naval Research in 1994 (Nittrouer and
80 Kravitz 1996), and the other is the Continental Slope Stability (COSTA)
81 project launched by the European Commission in 2000 (Mienert 2004).
82 These efforts provide instructive insights into the submarine processes of
83 sediment transport and slope stability through extensive interpretations of
84 post-failure scars and deposits. However, their episodic occurrences and
85 underwater development processes have never been observed. To provide
86 insights into the physical aspects, a few small-scale laboratory experiments
87 have been performed. The pioneering experiments are primarily focused on

88 the role of subaqueous debris flow in generating turbidity current (Hampton
89 1972; Marr et al. 2001; Mohrig and Marr 2003). Recent experiments are
90 conducted to unravel the characteristics of their mobility. The phenomenon
91 of hydroplaning (Mohrig et al. 1998, 1999; Toniolo et al. 2004) and soil
92 softening (Ilstad et al. 2004a, b) are successfully observed. The mechanisms
93 provide possible explanations for long runout distances of many submarine
94 debris flows on very gentle continental slopes. Ilstad et al. (2004c) first
95 observed the out-runner block, which illustrates the outermost deposition
96 patterns in many field cases. In addition, White et al. (2016) set up a series
97 of experiments to simulate the movement of submarine debris flows in the
98 geotechnical drum centrifuge. The experiments allow the mass movement to
99 commence with in-situ intact states and gradually transit into fluidized
100 conditions in subsequent runout.

101 With abundant datasets gathered from field investigations and laboratory
102 experiments, several one-dimensional analytical (Huang and García 1997,
103 1998, 1999) and numerical (BING, Imran et al. 2001) models have been
104 developed. However, they are limited to subaerial and non-hydroplaning
105 subaqueous muddy debris flows. Several extensions of the BING model are

106 introduced: presence of isolated intact blocks (B-BING, De Blasio et al.
107 2004a), linear increase of yield strength with thickness due to consolidation
108 (C-BING, De Blasio et al. 2004a), hydroplaning (W-BING, De Blasio et al.
109 2004b), and soil softening (R-BING, De Blasio et al. 2005). Gauer et al.
110 (2005, 2006) used the commercial Computational Fluid Dynamics (CFD)
111 software ANSYS CFX to perform a series of back-calculations of laboratory
112 experiments as well as replicate retrogressive failures of the Storegga slide.
113 Spinewine et al. (2013) presented a Center-of-Mass approach to model the
114 trajectory, runout distance, and frontal velocity of density flow. However,
115 one of the limitations of these models is that they are one-dimensional, thus
116 failing to account for the lateral spreading of debris flow. To consider the
117 lateral spreading of debris flow, Niedoroda et al. (2006) developed a two-
118 dimensional Eulerian gridded debris flow model. White et al. (2016)
119 proposed a depth-averaged program UWA-SM^4 using the Smoothed Particle
120 Hydrodynamics (SPH) Method. Ingarfield et al. (2016) introduced two more
121 programs, i.e. the SM3+^{1} and the SWDF2D. The program SM3+^{1} is an
122 extension of UWA-SM^4, and the model SWDF2D is based on the Finite
123 Volume Method (FVM).

With increased activities in offshore drilling and mining pushing towards deeper water, prediction and evaluation of submarine debris flow associated geohazards are becoming increasingly important, which demands to advance the state of our current knowledge. In this work, a two-dimensional depth-averaged numerical model is developed to simulate downslope movement of subaqueous and subaerial debris flows. To demonstrate its effectiveness, the numerical model is applied to a series of one-dimensional laboratory and field environments (Wright and Krone 1987; Mohrig et al. 1999; Pirmez et al. 2004) as well as two-dimensional synthetic field-scale scenarios of subaqueous and subaerial muddy debris flows.

Model Descriptions

Equations for Rheological Model

To simulate the movement of submarine debris flows, a proper viscoplastic model should be selected to describe their rheological properties. In this work, the nonlinear Herschel-Bulkley model (Herschel and Bulkley 1926) is used to describe the rheology of debris flows. The rheological model is expressed as

$$\begin{cases} \tau = \tau_Y + K\left|\dfrac{\partial u}{\partial z}\right|^n & \left|\dfrac{\partial u}{\partial z}\right| > 0 \\ \tau \le \tau_Y & \left|\dfrac{\partial u}{\partial z}\right| = 0 \end{cases} \tag{1}$$

where τ is the internal shear stress (Pa), τ_Y is the yield stress (Pa), u is the velocity parallel to bed (m/s), z is the coordinate normal to bed, K is the consistency related to the dynamic viscosity μ (Pa·s), and $n \in (0,1.0]$ is the model factor for shear thinning fluid. When $n = 1.0$, the nonlinear Herschel-Bulkley model is simplified into the linear Bingham model.

In the Herschel-Bulkley model, it is assumed that debris flows come to a complete stop when their height reduces below a certain depth, which is termed as the critical depth (e.g., Marr et al. 2002; Parsons et al. 2007). The critical depth of debris flows is mainly associated with their rheology and the slope angle, and formulated as

$$h_c = \frac{\tau_Y}{(\rho_d - \rho_w) g \left|\dfrac{\partial \eta}{\partial x}\right|} \tag{2}$$

where h_c is the critical depth (m), ρ_d is the density of debris flows (kg/m^3), ρ_w is the density of ambient fluids (kg/m^3), g is the gravitational

155 acceleration (m/s^2), η is the bed elevation (m), and x is the coordinate
156 parallel to bed.

157 ***Equations for Debris Flow Movement***

158 Several assumptions are made in establishing the constitutive equations. A
159 thin layer approximation is applied, which represents that runout distances of
160 debris flows are much larger than the depth. The buoyancy effect of ambient
161 fluid on debris flows is considered. However, no mass fluxes and friction
162 interactions at the interface of debris flows and ambient fluid are assumed.
163 As a result, whether ambient fluid is water or air, debris flows are simplified
164 as the motion of one single phase. The conservation equation of mass is

165 $$\frac{\partial H}{\partial t}+\frac{\partial UH}{\partial x}+\frac{\partial VH}{\partial y}=M \tag{3}$$

166 and the conservation equations of momentum along x and y directions are

167 $$\frac{\partial UH}{\partial t}+\frac{\partial UUH}{\partial x}+\frac{\partial UVH}{\partial y}+\frac{1}{2}\frac{\rho_d-\rho_w}{\rho_d}g\frac{\partial H^2}{\partial x}+\frac{\rho_d-\rho_w}{\rho_d}gH\frac{\partial \eta}{\partial x}+\frac{\tau_{bx}}{\rho_d}=\frac{\mu}{\rho_d}\left(\frac{\partial^2 UH}{\partial x^2}+\frac{\partial^2 UH}{\partial y^2}\right) \tag{4a}$$

168
$$\frac{\partial VH}{\partial t}+\frac{\partial VUH}{\partial x}+\frac{\partial VVH}{\partial y}+\frac{1}{2}\frac{\rho_d-\rho_w}{\rho_d}g\frac{\partial H^2}{\partial y}+\frac{\rho_d-\rho_w}{\rho_d}gH\frac{\partial \eta}{\partial y}+\frac{\tau_{by}}{\rho_d}=\frac{\mu}{\rho_d}\left(\frac{\partial^2 VH}{\partial x^2}+\frac{\partial^2 VH}{\partial y^2}\right) \quad (4b)$$

169 where t is the time (s), x and y are the coordinates parallel to bed, U and
170 V are the depth-averaged velocities in x and y directions (m/s), H is the
171 height of debris flows (m), τ_{bx} and τ_{by} are the bottom shear stresses in x and
172 y directions (Pa), and M is the rate of flow per unit area (m/s).

173 ***Equations for Bottom Shear Stress***

174 The shear stress within debris flows is assumed to be linearly distributed.
175 The mixtures of particle materials and friction interactions between debris
176 flows and ambient fluid are ignored. Under these constraints, the internal
177 shear stress is presented in the form of

178
$$\tau=\tau_b\left(1-\frac{z}{H}\right) \quad (5)$$

179 where τ_b is the bottom shear stress (Pa).

180 Based on the assumptions in the Herschel-Bulkley model, debris flows
181 come to a complete stop when the height reduces below critical depth. On
182 the other hand, when the height is larger than critical depth, debris flows will

183 be driven by gravity to move down along the slope. The propagating debris
184 flows are assumed to be divided into two distinct parts, i.e. the shear and
185 plug layers [Fig. 1]. In the shear layer, shear stress exceeds yield stress, and
186 a parabolic velocity profile is presented. However, the plug layer shows a
187 uniform velocity. To determine the bottom shear stress, a non-dimensional
188 parameter ξ is introduced as

189 $$\xi = \frac{H_p}{H} = \frac{\tau_Y}{\tau_b}, \xi \in (0,1) \tag{6}$$

190 where H_p is the thickness of plug layer (m).

191 In the shear layer $z \in [0, H_s]$, the combination of Eq. (1) and Eq. (5)
192 yields

193 $$\tau_Y + K\left|\frac{\partial u}{\partial z}\right|^n = \tau_b\left(1 - \frac{z}{H}\right) \tag{7}$$

194 where H_s is the thickness of shear layer (m). With the assumption of no-slip
195 conditions at bottom, i.e. $U(0) = 0$, the depth-dependent velocity is derived
196 as

197 $$u(z)=-\frac{KH}{\tau_b}\frac{\left(\frac{\tau_b-\tau_Y}{K}-\frac{\tau_b}{KH}z\right)^{\frac{1}{n}+1}}{\frac{1}{n}+1}+\frac{H}{\tau_b}\frac{(\tau_b-\tau_Y)^{\frac{1}{n}+1}}{\left(\frac{1}{n}+1\right)K^{\frac{1}{n}}},z\in[0,H_s] \quad (8)$$

198 In the plug layer $z\in[H_s,H]$, the depth-dependent velocity is expressed

199 as

200 $$u(z)=-\frac{KH}{\tau_b}\frac{\left(\frac{\tau_b-\tau_Y}{K}-\frac{\tau_b}{KH}H_s\right)^{\frac{1}{n}+1}}{\frac{1}{n}+1}+\frac{H}{\tau_b}\frac{(\tau_b-\tau_Y)^{\frac{1}{n}+1}}{\left(\frac{1}{n}+1\right)K^{\frac{1}{n}}},z\in[H_s,H] \quad (9)$$

201 The depth averaged velocity U is obtained with

202 $$U=\frac{\int_0^H u(z)dz}{H}=\frac{\int_0^{H_s}u(z)dz+\int_{H_s}^H u(z)dz}{H} \quad (10)$$

203 Finally, substitution of Eq. (8) and Eq. (9) into Eq. (10) leads to

204 $$\left(\xi+\frac{1}{n}+1\right)(1-\xi)^{\frac{1}{n}+1}-\frac{\left(\frac{1}{n}+1\right)\left(\frac{1}{n}+2\right)|U|K^{\frac{1}{n}}}{H\tau_Y^{\frac{1}{n}}}\xi^{\frac{1}{n}}=0,\xi\in(0,1) \quad (11)$$

205 This equation can be further simplified with $n=1.0$ for the Bingham

206 model, which presents the same mathematical representation as derived by

207 Pastor et al. (2004). This equation leads to a unique solution ξ with respect

208 to the specific range of $\xi \in (0,1)$. The Newton-Raphson iteration method is

209 used to solve the equation.

210 **Numerical Schemes**

211 The explicit finite difference method is used to solve the constitutive

212 equations. The time derivative terms are discretized using the forward

213 scheme, and other terms such as the convection, diffusion, and pressure

214 terms are discretized using the central difference scheme. When $q_x = UH$

215 and $q_y = VH$, the conservation equations of momentum in x and y

216 directions as well as the conservation equation of mass are discretized at

217 (i, j) as

218
$$\begin{aligned}
&\frac{q_{xi,j}^{n+1} - Q\left(q_{xi,j}^{n}\right)}{\Delta t} + \frac{\left(Uq_x\right)_{i+1,j}^{n} - \left(Uq_x\right)_{i-1,j}^{n}}{2\Delta x} + \frac{\left(Uq_y\right)_{i,j+1}^{n} - \left(Uq_y\right)_{i,j-1}^{n}}{2\Delta y} + \\
&\frac{1}{2}\frac{\rho_d - \rho_w}{\rho_d} g \frac{\left(H^2\right)_{i+1,j}^{n} - \left(H^2\right)_{i-1,j}^{n}}{2\Delta x} + \frac{\rho_d - \rho_w}{\rho_d} g H_{i,j}^{n} \frac{\eta_{i+1,j} - \eta_{i-1,j}}{2\Delta x} + \\
&\mathrm{sgn}\left(U_{i,j}^{n}\right)\frac{\tau_{bx}\left(U_{i,j}^{n}, H_{i,j}^{n}, \tau_Y, \mu\right)}{\rho_d} = \frac{\mu}{\rho_d}\left(\frac{q_{xi+1,j}^{n} - 2q_{xi,j}^{n} + q_{xi-1,j}^{n}}{\Delta x^2} + \frac{q_{xi,j+1}^{n} - 2q_{xi,j}^{n} + q_{xi,j-1}^{n}}{\Delta y^2}\right)
\end{aligned} \tag{12a}$$

$$\frac{q_{yi,j}^{n+1}-Q\left(q_{yi,j}^{n}\right)}{\Delta t}+\frac{\left(Vq_x\right)_{i+1,j}^{n}-\left(Vq_x\right)_{i-1,j}^{n}}{2\Delta x}+\frac{\left(Vq_y\right)_{i,j+1}^{n}-\left(Vq_y\right)_{i,j-1}^{n}}{2\Delta y}+$$

$$\frac{1}{2}\frac{\rho_d-\rho_w}{\rho_d}g\frac{\left(H^2\right)_{i,j+1}^{n}-\left(H^2\right)_{i,j-1}^{n}}{2\Delta y}+\frac{\rho_d-\rho_w}{\rho_d}gH_{i,j}^{n}\frac{\eta_{i,j+1}-\eta_{i,j-1}}{2\Delta y}+ \tag{12b}$$

$$\operatorname{sgn}\left(V_{i,j}^{n}\right)\frac{\tau_{by}\left(V_{i,j}^{n},H_{i,j}^{n},\tau_Y,\mu\right)}{\rho_d}=\frac{\mu}{\rho_d}\left(\frac{q_{yi+1,j}^{n}-2q_{yi,j}^{n}+q_{yi-1,j}^{n}}{\Delta x^2}+\frac{q_{yi,j+1}^{n}-2q_{yi,j}^{n}+q_{yi,j-1}^{n}}{\Delta y^2}\right)$$

$$\frac{H_{i,j}^{n+1}-Q\left(H_{i,j}^{n}\right)}{\Delta t}+\frac{q_{xi+1,j}^{n+1}-q_{xi-1,j}^{n+1}}{2\Delta x}+\frac{q_{yi,j+1}^{n+1}-q_{yi,j-1}^{n+1}}{2\Delta y}=M_{i,j}^{n} \tag{12c}$$

where Δt is the time step (s), Δx and Δy are the grid sizes (m), and q_x and q_y are the mass fluxes per unit width (m^2/s). To make solutions in each time step convergent and to avoid the dispersive effect, the following novel functions are introduced as (Han et al. 2015)

$$Q\left(q_{xi,j}^{n}\right)=\left(1-CFL\right)q_{xi,j}^{n}+CFL\frac{q_{xi+1,j}^{n}+q_{xi-1,j}^{n}+q_{xi,j+1}^{n}+q_{xi,j-1}^{n}}{4} \tag{13a}$$

$$Q\left(q_{yi,j}^{n}\right)=\left(1-CFL\right)q_{yi,j}^{n}+CFL\frac{q_{yi+1,j}^{n}+q_{yi-1,j}^{n}+q_{yi,j+1}^{n}+q_{yi,j-1}^{n}}{4} \tag{13b}$$

$$Q\left(H_{i,j}^{n}\right)=\left(1-CFL\right)H_{i,j}^{n}+CFL\frac{H_{i+1,j}^{n}+H_{i-1,j}^{n}+H_{i,j+1}^{n}+H_{i,j-1}^{n}}{4} \tag{13c}$$

where *CFL* is the Courant-Friedrichs-Lewy condition. The *CFL* condition provides a criterion for the convergence of explicit numerical models. It implies that time step must be less than a certain value to produce correct

231 results (Courant et al. 1928). To maintain the stability of numerical solutions,
232 the *CFL* condition should satisfy the criterion $CFL < 1$, and the value of
233 *CFL* condition is given as (Beguería et al. 2009)

234 $$CFL = \frac{\Delta t}{\Delta x} \max\left(U, V\right) \tag{14}$$

235 **Model Verifications**

236 ***Verification with One-dimensional Laboratory Tests (Wright and Krone***
237 ***1987)***

238 The numerical model is first applied to the laboratory tests conducted by
239 Wright and Krone (1987) in subaerial environments. The same experimental
240 data was used by previous researchers to verify their analytical (Huang and
241 García 1997) and numerical (Imran et al. 2001) models. As such, the input
242 parameters are consistent with the settings in previous validation work. The
243 debris flow is assumed to be the Bingham fluid. The yield stress is 42.5 Pa,
244 and the dynamic viscosity is 0.22 Pa·s. The densities of debris flow and
245 ambient air are 1073.0 kg/m^3 and 1.0 kg/m^3, respectively. The geometry of
246 initial failure mass presents a cuboid with its length of 1.8 m, height of 0.3 m,
247 and nominal width of 0.16 m. An inclined channel with dimensions of 15.0

248 m in length and 2.0 m in width is schematized [Fig. 2]. The channel bed has
249 a constant slope of 0.06. The space step is set as 0.01 m, and time step is
250 0.001 s. The comparison of deposit thicknesses of debris flow between the
251 numerical and experimental results is shown [Fig. 3]. The modelling results
252 show agreement with the laboratory observations. However, the location of
253 the forefront of debris flow is slightly underestimated. This might due to the
254 backward movement of debris flow.

255 ***Verification with One-dimensional Laboratory Tests (Mohrig et al. 1999)***

256 The present model is also applied to the laboratory experiments conducted
257 by Mohrig et al. (1999) in subaerial settings. For numerical exercises, an
258 inclined channel with its length of 15.0 m and width of 2.0 m is set [Fig. 4].
259 The channel is segmented with a slope break located at 10.7 m away from
260 the upstream boundary. The upper and lower slope angles are set as 6° and
261 1°. Runs 2a and 3a represent the subaerial scenarios in Mohrig et al. (1999)
262 laboratory experiments. Herein, the input parameters of the numerical model
263 are set to be the same as measured in the laboratory experiments. The debris
264 flow is also treated as the Bingham fluid. The densities of debris flow and
265 ambient air are set as 1600.0 kg/m^3 and 1.3 kg/m^3. For the run 2a, the yield

266 stress is 49.0 Pa, and the dynamic viscosity is 0.035 Pa·s. However, for the
267 run 3a, they are 36.0 Pa and 0.023 Pa·s. A summary of parameter settings is
268 listed in Table 1. Since all other input parameters are directly determined
269 from Mohrig et al. (1999) laboratory experiments, only the dimensions of
270 initial failure mass are unknown, and thus will be used here to calibrate the
271 numerical model. Herein, a cuboid of debris flow is set as the initial failure
272 mass. The length, width, and height of cuboid are calibrated in the numerical
273 model for each run to agree with the laboratory experiments. The calibrated
274 dimensions of cuboid for each run are also given in Table 1. Comparisons of
275 deposit thickness between the numerical and experimental results for each
276 run are shown [Fig. 5]. It is shown that the modelling results of deposit
277 thickness for each run agree with the experimental measurements. However,
278 their frontal velocities are slightly overestimated [Fig. 6]. This is due to the
279 augmented momentum arising from immediate release of cuboid of debris
280 mass at a time. In the laboratory experiments, the debris mass is gradually
281 released from the upstream reservoir through a slot into the flume. Note that
282 the left peak of frontal velocity in Fig. 6 is due to the backflow towards
283 upstream.

284 ***Verification with Field Environment (Pirmez et al. 2004)***

285 The previous efforts of model verifications are based on the one-dimensional
286 laboratory tests (Wright and Krone 1987; Mohrig et al. 1999). In this part,
287 one more model verification is conducted with the field environment, i.e. the
288 Na Kika Basin, Gulf of Mexico (Pirmez et al. 2004). Two debris flow
289 deposits are identified and named as Unit CD and Surficial DF [Fig. 7]. The
290 Surficial DF has no sediment cover above it, whereas the Unit CD is buried
291 by 15 m of acoustically stratified sediments. The black lines represent the
292 thalweg along the canyons, and the bathymetry profile L1 is given [Fig. 8].
293 The present numerical model is used to reproduce sediment failure scenarios
294 leading to the two existing debris flow deposits. As such, two simulations
295 are performed with the bathymetry profile L1. The debris flow is also
296 assumed as Bingham fluid. The parameter settings are consistent with the
297 recommendations of Pirmez et al. (2004). In both simulations, the density of
298 debris flow is 1600 kg/m^3, and its dynamic viscosity is 2 Pa·s. In the
299 simulation of Unit CD, the position of initial failure mass starts from 9.1 km
300 to 19.1 km. The thickness of initial failure mass is 140 m. The distal position
301 of Unit CD is at 108 km. To reach the same distal position, the yield stress

302 of debris flow is calibrated to be 1600 Pa. This value is in accordance with
303 estimations for deeper sediment (1200 Pa - 4800 Pa). However, in the case
304 of Surficial DF, the initial failure mass stretches from 73.8 km to 76.8 km.
305 The initial failure thickness is 30 m. The distal position of Surficial DF is
306 86.5 km. The yield stress is calibrated as 700 Pa, which also conforms to the
307 recommendations for shallower sediment (300 Pa - 1400 Pa). The modelling
308 results for each simulation are compared with the available sediment core
309 information [Fig. 9]. It is shown that, for both simulations, the runout
310 distances reach the measured distal positions of debris flow deposits.
311 However, based on current available borehole data, the modelling results
312 overestimate the deposit thicknesses of debris flow at their distal positions.
313 This is probably due to exclusion of hydroplaning (Mohrig et al. 1998, 1999;
314 Toniolo et al. 2004) and soil softening (Ilstad et al. 2004a, b) of submarine
315 debris flow in the present model. Direct reduction of yield stress of debris
316 flow will be conducive to reach long runout distances as field observations.
317 However, this will lead to underestimation of deposit thickness of debris
318 flow on the upper slope, and overestimation at the distal position.
319

Model Applications

Application to Two-dimensional Continental Shelf with a Uniform Slope

The present model is further applied to the schematized continental shelf with a uniform slope [Fig. 10]. The distance along the shoreline is 1500 m, and the downslope length of the schematized domain is 500 m. The angle of the uniform slope is set to be 6°. The initial failure shape is a cuboid with its centroid located at (125 m, 750 m). The width and length of the cuboid are the same and set as 100 m, and the thickness is 4 m. The debris flow is characterized as the Bingham fluid with yield stress of 200 Pa and dynamic viscosity of 58 Pa·s (Das 2012). The bulk density of debris flow is 1450 kg/m^3. The time step is set as 0.001 s, and space step is 5 m. The deposition patterns at time interval of 10 s running for a total time of 50 s are shown [Fig. 11]. The debris mass is initially placed on the uniform slope. Upon release, debris mass spreads out all around but will dominantly propagate toward downslope.

Sensitivity analyses are performed to study the influence of yield stress, dynamic viscosity, slope angle, and initial failure height on runout distances of debris flow. The runout distances are taken as the length between the

forefront of initial and final debris deposits. When studying the effects of yield stress and dynamic viscosity on runout distances of debris flow, the slope angle is set as 6˚, and the initial failure height is 4m. The yield stress varies from 200 Pa to 1400 Pa, and the dynamic viscosity ranges between 58 Pa·s to 208 Pa·s. A summary of all parameter settings is listed in Table 2. It is shown that the runout distance significantly increases when decreasing the yield stress, and it slightly decreases when increasing the dynamic viscosity [Fig. 12]. The yield stress has much more control over the runout distance than the dynamic viscosity. The dynamic viscosity has an increasing impact on the runout distance when the yield stress becomes lower. Similarly, when studying the effects of slope angle and initial failure height on the runout distances of debris flow, the yield stress is set as 200 Pa, and the dynamic viscosity is 58 Pa·s. The slope angle varies from 3˚ to 6˚, and the initial failure height ranges between 1.5 m to 4.0 m. A summary of the parameter settings is listed in Table 3. It is shown that both the initial failure height and the slope angle have significant influences on the runout distance [Fig. 13]. The long runout distance is achieved with steep slope and high initial failure height.

356 In addition, the effect of initial failure shapes on the runout distance of
357 debris flow is also explored. When studying the influence of initial failure
358 shapes on the runout distance, two additional initial failure shapes, i.e. the
359 hemisphere and semi-ellipsoid, are considered. The coordinate of the center
360 is (125 m, 750 m), which overlaps with that of cuboid. The total volume of
361 both the hemisphere and semi-ellipsoid is 40000 m^3, which is consistent
362 with that of the cuboid. With known volume, the radius of hemisphere is
363 calculated to be 26.7 m. For the semi-ellipsoid, the semi-principal axis of
364 length in the downslope direction is set to be 50 m, which is a half of the
365 cuboid length. The semi-principal axis of length in the lateral direction is 50
366 m, which is also half of the cuboid width. With known volume, the semi-
367 principal axis of length in z direction is calculated as 7.6 m. A summary of
368 parameter settings is displayed in Table 4. The deposition patterns for initial
369 failure shapes of cuboid, semi-ellipsoid, and hemisphere are shown [Fig.
370 14]. It is shown that initial failure shape of hemisphere generates the largest
371 runout distance of 480 m, whereas that of cuboid yields the smallest runout
372 distance of 420 m. The runout distance of debris flow increases by 14%.
373 This is because the initial failure shape of hemisphere has the largest initial

374 failure height, and the cuboid has the smallest initial failure height. It is
375 further demonstrated that the initial failure height is a controlling factor in
376 determining the runout distances of debris flow.

377 ***Application to Two-dimensional Continental Shelf with a Sinuous Canyon***

378 The numerical model is finally applied to the schematized continental shelf
379 with sinuous canyons of two different dimensions [Fig. 15]. The midpoints
380 at the uppermost and lowermost boundaries are selected as the starting and
381 ending points of the thalweg of sinuous canyon. The thalweg of sinuous
382 canyon is represented by a sine function of one period. The wave length of
383 the landform is 500 m, and the wave amplitude is 100 m. The symmetrical
384 cross-section of canyon is V-shaped with a constant side slope angle. The
385 side slope angle is determined by the ratio of depth at the thalweg and
386 horizontal distance of deviation from the thalweg. In Fig. 15(a), the depth at
387 the thalweg is 5 m, and the horizontal deviation from the thalweg is 50 m. In
388 Fig. 15(b), the depth at the thalweg and the horizontal deviation from the
389 thalweg are respectively 15 m and 150 m. Variations in deposition patterns
390 are observed in the two sinuous canyons with different dimensions [Fig. 16].
391 It is shown that the debris mass overflows the canyon with smaller scale,

392 whereas it is confined within the canyon with larger scale. The debris mass
393 flowing within the canyon is primarily travelling along the thalweg, which
394 further demonstrate the capability of the model.

395 **Discussions and Conclusions**

396 A two-dimensional numerical model is developed to simulate the motions of
397 subaqueous and subaerial muddy debris flows. The numerical model is
398 verified with one-dimensional laboratory experiments in subaerial settings
399 (Wright and Krone 1987; Mohrig et al. 1999), and subaqueous debris flows
400 in field settings (Pirmez et al. 2004). Modelling results show agreement with
401 the laboratory and field observations. Two-dimensional model applications
402 are performed with two schematized continental slopes, i.e. a uniform slope
403 and a sinuous canyon. For the scenario with a uniform slope, sensitivity
404 analyses are performed to explore the relative importance of yield stress,
405 dynamic viscosity, bottom slope, initial failure height, and initial failure
406 shape for the runout distances of debris flow. It is found that yield stress,
407 bottom slope, and initial failure height are controlling factors in determining
408 the runout distances of debris flow. For scenario with a sinuous canyon, two

409 different dimensions of the canyon are further used to show the capability of
410 the present model.

411 The limitation of the present numerical model is observed. The effects of
412 hydroplaning (Mohrig et al. 1998, 1999; Toniolo et al. 2004) and soil
413 softening (Ilstad et al. 2004a, b) are not taken into account. This leads to the
414 failure of model applications to reach long runout distances in Mohrig et al.
415 (1999) subaqueous runs 2w and 3w [Fig. 17]. Herein, to reach long runout,
416 the additional runs 2wr and 3wr are synthesized with reduced yield stress.
417 The summary of parameter settings for runs 2w, 3w, 2wr, and 3wr is also
418 listed in Table 1. However, it produces an excessive bulk of debris deposits
419 at the forefront and inadequate depositions on the upper slope [Fig. 17]. As
420 such, the present numerical model is limited to the subaqueous debris flows
421 without hydroplaning or soil softening. Despite this limitation of present
422 model, it can still serve as an effective geo-hazard evaluation tool for the
423 purpose of mass gravity flow analyses.

424 **Acknowledgements**

425 This research work was primarily supported by the U.S. Army Research
426 Office [Grant No. W911NF1310128] and the Fugro Inc. [Grant No.

636567]. Partial financial supports were also provided by the Coastal Hazards Center of Excellence and the Institute for Multimodal Transportation at Jackson State University, and are greatly appreciated.

References

Beguería, S., Van Asch, T.W.J., Malet, J.P., and Gröndahl, S. (2009). "A GIS-based numerical model for simulating the kinematics of mud and debris flows over complex terrain." *Nat. Hazards Earth Syst. Sci.*, 9, 1897–1909.

Bjerrum, L. (1971). "Subaqueous slope failure in Norwegian Fjords." *Norwegian. Geotechnical Institute (NGI) Publication*, 88, 1–8.

Bruschi, R., Bughi, S., Spinazzè, M., Torselletti, E., and Vitali, L. (2006). "Impact of debris flows and turbidity currents on seafloor structures." *Norw. J. Geol.*, 86, 317–337.

Canals, M., Lastras, G., Urgeles, R., Casamor, J.L., Mienert, J., Cattaneo, A., De Batist, M., Haflidason, H., Imbo, Y., Laberg, J.S., Locat, J., Long, D., Longva, O., Masson, D.G., Sultan, N., Trincardi, F., and Bryn, P. (2004). "Slope failure dynamics and impacts from seafloor and

444 shallow sub-seafloor geophysical data: case studies from the COSTA
445 project." *Mar. Geol.*, 213, 9–72.
446 Courant, R., Friedrichs, K., and Lewy, H. (1928). "Über die partiellen
447 Differenzengleich-ungen der mathematischen Physik." *Math. Ann.*, 100
448 (1), 32–74.
449 Das, H.S. (2012). "Mass gravity flow analyses (Gorgon expansion project)."
450 *Report to Fugro Corporation*, March 2012.
451 De Blasio, F.V., Elverhøi, A., Issler, D., Harbitz, C.B., Bryn, P., and Lien,
452 R. (2004a). "Flow models of natural debris flows originating from over
453 consolidated clay materials." *Mar. Geol.*, 213, 439–455.
454 De Blasio, F.V., Elverhøi, A., Issler, D., Harbitz, C.B., Bryn, P., and Lien,
455 R. (2005). "On the dynamics of subaqueous clay rich gravity mass
456 flows-the giant Storegga slide, Norway." *Mar. Petrol. Geol.*, 22, 179–
457 186.
458 De Blasio, F.V., Engvik, L., Harbitz, C.B., and Elverhøi, A. (2004b).
459 "Hydroplaning and submarine debris flows." *J. Geophys. Res.*, 109,
460 C01002.

461 Denlinger, R.P., and Iverson, R.M. (2001). “Flow of variably fluidized
462 granular masses across three-dimensional terrain: 2. numerical
463 predictions and experimental tests.” *J. Geophys. Res.*, 106(B1), 553–566.
464 Elverhøi, A., Harbitz, C.B., Dimakis, P., Mohrig, D., Marr, J., and Parker, G.
465 (2000). “On the dynamics of subaqueous debris flows.” *Oceanography*,
466 13(3), 109–117.
467 Fine, I.V., Rabinovich, A.B., Bornhold, B.D., Thomson, R.E., and Kulikov,
468 E.A. (2005). “The Grand Banks landslide-generated tsunami of
469 November 18, 1929: preliminary analysis and numerical modeling.”
470 *Mar. Geol.*, 215, 45–57.
471 Gauer, P., Elverhøi, A., Issler, D., and De Blasio, F.V. (2006). “On
472 numerical simulations of subaqueous slides: back-calculations of
473 laboratory experiments.” *Norw. J. Geol.*, 86, 295–300.
474 Gauer, P., Kvalstad, T.J., Forsberg, C.F., Bryn, P., and Berg, K. (2005).
475 “The last phase of the Storegga Slide: simulation of retrogressive slide
476 dynamics and comparison with slide-scar morphology.” *Mar. Petrol.*
477 *Geol.*, 22, 171–178.

478 Hampton, M.A. (1972). “The role of subaqueous debris flow in generating
479 turbidity currents.” *J. Sediment. Petrol.*, 42(4), 775–793.
480 Hampton, M.A., and Locat, J. (1996). “Submarine landslides.” *Rev.*
481 *Geophys.*, 34(1), 33–59.
482 Han, Z., Chen, G., Li, Y., Tang, C., Xu, L., He, Y., Hang, X., and Wang, W.
483 (2015). “Numerical simulation of debris-flow behavior incorporating a
484 dynamic method for estimating the entrainment.” *Eng. Geol.*, 190, 52–
485 64.
486 Herschel, W.H., and Bulkley, R. (1926). "Konsistenzmessungen von
487 Gummi-Benzollösungen." *Kolloid Zeitschrift*, 39, 291–300.
488 Huang, X., and García, M.H. (1997). “A perturbation solution for Bingham-
489 plastic mudflows.” *J. Hydraul. Eng.*, 123(11), 986–994.
490 Huang, X., and García, M.H. (1998). “A Herschel-Bulkley model for mud
491 flow down a slope.” *J. Fluid Mech.*, 374, 305–333.
492 Huang, X., and García, M.H. (1999). “Modelling of non-hydroplaning
493 mudflows on continental slopes.” *Mar. Geol.*, 154, 131–142.
494 Hungr, O. (1995). “A model for the runout analysis of rapid flow slides,
495 debris flows, and avalanches.” *Can. Geotech. J.*, 32(4), 610–623.

496 Ilstad, T., De Blasio, F.V., Elverhøi, A., Harbitz, C.B., Engvik, L., Longva,
497 O., and Marr, J.G. (2004c). "On the frontal dynamics and morphology of
498 submarine debris flows." *Mar. Geol.*, 213, 481–497.
499 Ilstad, T., Elverhøi, A., Issler, D., and Marr, J.G. (2004b). "Subaqueous
500 debris flow behavior and its dependence on the sand/clay ratio: a
501 laboratory study using particle tracking." *Mar. Geol.*, 213, 415–438.
502 Ilstad, T., Marr, J.G., Elverhøi, A., and Harbitz, C.B. (2004a). "Laboratory
503 studies of subaqueous debris flows by measurements of pore-fluid
504 pressure and total stress." *Mar. Geol.*, 213, 403–414.
505 Imran, J., Parker, G., Locat, J., and Lee, H. (2001). "1D numerical model of
506 muddy subaqueous and subaerial debris flows." *J. Hydraul. Eng.*, 27(6),
507 717–729.
508 Ingarfield, S., Sfouni-Grigoriadou, M., de Brier, C., and Spinewine, B.
509 (2016). "The importance of soil characterization in modelling sediment
510 density flows." *Proc., Offshore Technology Conf.*, Offshore Technology
511 Conference, Houston.

512 Iverson, R.M., and Denlinger, R.P. (2001). “Flow of variably fluidized
513 granular masses across three-dimensional terrain: 1. coulomb mixture
514 theory.” *J. Geophys. Res.*, 106 (B1), 537–552.
515 Jiang, L., and Le Blond, P.H. (1992). “The coupling of a submarine slide
516 and the surface waves which it generates.” *J. Geophys. Res.*, 97(C8),
517 12731–12744.
518 Jiang, L., and Le Blond, P.H. (1993). “Numerical modeling of an underwater
519 Bingham plastic mudslide and the waves which it generates.” *J.*
520 *Geophys. Res.*, 98(C6), 10303–10317.
521 Jiang, L., and Le Blond, P. H. (1994). “Three-dimensional modeling of
522 tsunami generation due to a submarine mudslide.” *J. Phys. Oceanogr.*,
523 24, 559–572.
524 Lee, H.J., Locat, J., Desgagnes, P., Parsons, J.D., McAdoo, B.G., Orange,
525 D.L., Puig, P., Wong, F.L., Dartnell, P., and Boulanger, E. (2007).
526 “Submarine mass movements on continental margins.” *Continental*
527 *Margin Sedimentation: From Sediment Transport to Sequence*
528 *Stratigraphy (eds. Nittrouer, C.A., Austin, J.A., Field, M.E., Kravitz,*

529 *J.H., Syvitski, J.P.M., and Wiberg, P.L.)*, Blackwell Publishing Ltd.,
530 Oxford, UK.
531 Marr, J.G., Elverhoi, A., Harbitz, C., Imran, J., and Harff, P. (2002).
532 "Numerical simulation of mud-rich subaqueous debris flows on the
533 glacially active margins of the Svalbard-Barents Sea." *Mar. Geol.*, 188,
534 351–364.
535 Marr, J.G., Harff, P.A., Shanmugam, G., and Parker, G. (2001).
536 "Experiments on subaqueous sandy gravity flows: the role of clay and
537 water content in flow dynamics and depositional structures." *Geol. Soc.*
538 *Am. Bull.*, 113(11), 1377–1386.
539 Masson, D.G., Harbitz, C.B., Wynn, R.B., Pedersen, G., and Løvholt, F.
540 (2006). "Submarine landslides: processes, triggers and hazard
541 prediction." *Philos. Trans. R. Soc. Lond. A*, 364(1845), 2009–2039.
542 McDougall, S., and Hungr, O. (2004). "A model for the analysis of rapid
543 landslide motion across three-dimensional terrain." *Can. Geotech. J.*,
544 41(6), 1084–1097.
545 Mienert, J. (2004). "COSTA-continental slope stability: major aims and
546 topics." *Mar. Geol.*, 213, 1–7.

547 Mohrig, D., Ellis, C., Parker, G., Whipple, K.X., and Hondzo, M. (1998).
548 "Hydroplaning of subaqueous debris flows." *Geol. Soc. Am. Bull.*,
549 110(3), 387–394.
550 Mohrig, D., Elverhøi, A., and Parker, G. (1999). "Experiments on the
551 relative mobility of muddy subaqueous and subaerial debris flows, and
552 their capacity to remobilize antecedent deposits." *Mar. Geol.*, 154, 117–
553 129.
554 Mohrig, D., and Marr, J.G. (2003). "Constraining the efficiency of turbidity
555 current generation from submarine debris flows and slides using
556 laboratory experiments." *Mar. Petrol. Geol.*, 20, 883–899.
557 Niedoroda, A.W., Reed, C.W., Das, H.S., Hatchett, J.L., and Perlet, A.B.
558 (2006). "Controls of the behavior of marine debris flows." *Norw. J.*
559 *Geol.*, 86(4), 265–274.
560 Nittrouer, C.A., and Kravitz, J.H. (1996). "STRATAFORM: a program to
561 study the creation and interpretation of sedimentary strata on continental
562 margins." *Oceanography*, 9(3), 146–152.
563 Parsons, J.D., Friedrichs, C.T., Traykovski, P.A., Mohrig, D., Imran, J.,
564 Syvitski, J.P.M., Parker, G., Puig, P., Buttles, J.L., and García, M.H.

(2007). “The mechanics of marine sediment gravity flows.” *Continental Margin Sedimentation: From Sediment Transport to Sequence Stratigraphy (eds. Nittrouer, C.A., Austin, J.A., Field, M.E., Kravitz, J.H., Syvitski, J.P.M., and Wiberg, P.L.)*, Blackwell Publishing Ltd., Oxford, UK.

Pastor, M., Quecedo, M., Gonzalez, E., Herreros, M.I., Merodo, J.A.F., and Mira, P. (2004). “Simple approximation to bottom friction for Bingham fluid depth integrated models.” *J. Hydraul. Eng.*, 130(2), 149–155.

Pirmez, C., Marr, J., Shipp, C., and Kopp, F. (2004). “Observations and numerical modeling of debris flows in the Na Kika Basin, Gulf of Mexico.” *Proc., Offshore Technology Conf.*, Offshore Technology Conference, Houston.

Remaître, A., Malet, J., Maquaire, O., Ancey, C., and Locat, J. (2005). “Flow behavior and run out modelling of a complex debris flow in a clay-shale basin.” *Earth Surf. Process. Landf.*, 30, 479–488.

Rzadkiewicz, S.A., Mariotti, C., and Heinrich, P. (1997). “Numerical simulation of submarine landslides and their hydraulic effects.” *J. Waterw. Port Coast. Ocean Eng.*, 123(4), 149–157.

583 Spinewine, B., Rensonnet, D., De Thier, T., Clare, M., Unterseh, G., and
584 Capart, H. (2013). "Numerical modeling of runout and velocity for slide-
585 induced submarine density flows - a building block of integrated
586 geohazards assessment for deepwater developments." *Proc., Offshore*
587 *Technology Conf.*, Offshore Technology Conference, Houston.
588 Talling, P.J., Wynn, R.B., Masson, D.G., Frenz, M., Cronin, B.T., Schiebel,
589 R., Akhmetzhanov, A.M., Dallmeier-Tiessen, S., Benetti, S., Weaver,
590 P.P.E., Georgiopoulou, A., Zuhlsdorff, C., and Amy, L.A. (2007).
591 "Onset of submarine debris flow deposition far from original giant
592 landslide." *Nature*, 450(22), 541–544.
593 Talling, P.J. (2014). "On the triggers, resulting flow types and frequencies of
594 subaqueous sediment density flows in different settings." *Mar. Geol.*,
595 352, 155–182.
596 Tappin, D.R. (2010). "Submarine mass failures as tsunami sources: their
597 climate control." *Philos. Trans. R. Soc. Lond. A*, 368, 2417–2434.
598 Toniolo, H., Harff, P., Marr, J., Paola, C., and Parker, G. (2004).
599 "Experiments on reworking by successive unconfined subaqueous and
600 subaerial muddy debris flows." *J. Hydraul. Eng.*, 130(1), 38–48.

White, D.J., Randolph, M.F., Gaudin, C., Boylan, N., Wang, D., Boukpeti, N., Zhu, H., and Sahdi, F. (2016). “The impact of submarine slides on pipelines: outcomes from the COFS-MERIWA JIP.” *Proc., Offshore Technology Conf.*, Offshore Technology Conference, Houston.

Wright, V., and Krone, R. (1987). "Laboratory and numerical study of mud and debris flows." *Proc., 22nd International Association for Hydraulic Research Congress*, Lausanne, Switzerland.

Yuan, F., Wang, L., Guo, Z., and Shi, R. (2012). “A refined analytical model for landslide or debris flow impact on pipelines. part I: surface pipelines.” *Appl. Ocean Res.*, 35, 95–104.

Zakeri, A., Høeg, K., and Nadim, F. (2008). “Submarine debris flow impact on pipelines-part I: experimental investigation.” *Coast. Eng.*, 55(12), 1209–1218.

Table 1. Parameter Settings for Various Runs

Run	Ambient density ρ_a (kg/m^3)	Debris density ρ_d (kg/m^3)	Viscosity μ_d (Pa·s)	Yield stress τ_Y (Pa)	Initial block L(m)×W(m)×H(m)
2a	1.3	1600.0	0.035	49.0	0.41×0.16×0.460
2w	1000.0	1600.0	0.035	49.0	0.41×0.16×0.460
2wr	1000.0	1600.0	0.035	6.7	0.41×0.16×0.460
3a	1.3	1600.0	0.023	36.0	0.41×0.16×0.365
3w	1000.0	1600.0	0.023	36.0	0.41×0.16×0.365
3wr	1000.0	1600.0	0.023	4.9	0.41×0.16×0.365

628 **Table 2.** Input Parameters for Studying the Effects of Yield Stress and
629 Dynamic Viscosity on the Runout Distance

Case No.	Yield stress (Pa)	Dynamic viscosity (Pa·s)	Initial height (m)	Slope angle (˚)	Runout distance (m)
1	200	58	4	6	410
2	600	58	4	6	305
3	1000	58	4	6	230
4	1400	58	4	6	173
5	200	108	4	6	376
6	600	108	4	6	285
7	1000	108	4	6	220
8	1400	108	4	6	159
9	200	158	4	6	353
10	600	158	4	6	275
11	1000	158	4	6	210
12	1400	158	4	6	159
13	200	208	4	6	332
14	600	208	4	6	261
15	1000	208	4	6	203
16	1400	208	4	6	156

630
631
632
633
634
635

636 **Table 3.** Input Parameters for Studying the Effects of Slope Angle and

637 Initial Failure Height on the Runout Distance

Case No.	Yield stress (Pa)	Dynamic viscosity (Pa·s)	Initial height (m)	Slope angle (˚)	Runout distance (m)
17	200	58	4	6	410
18	200	58	4	5	376
19	200	58	4	4	336
20	200	58	4	3	288
21	200	58	3	6	359
22	200	58	3	5	315
23	200	58	3	4	285
24	200	58	3	3	241
25	200	58	2	6	281
26	200	58	2	5	258
27	200	58	2	4	210
28	200	58	2	3	183
29	200	58	1.5	6	224
30	200	58	1.5	5	203
31	200	58	1.5	4	169
32	200	58	1.5	3	146

638

639

640

641

642

643

644 **Table 4.** Input Parameters for Studying the Effects of Initial Failure Shapes

645 on the Runout Distance

Initial deposit shape	Characteristic length (m)		Total volume (m^3)	
Cuboid	L	100	LWH	40000
	W	100		
	H	4		
Semi-ellipsoid	A	50	$2\pi ABC/3$	40000
	B	50		
	C	7.6		
Hemisphere	R	26.7	$2\pi R^3/3$	40000

646

Fig. 1

Click here to download Figure Fig. 1.tif

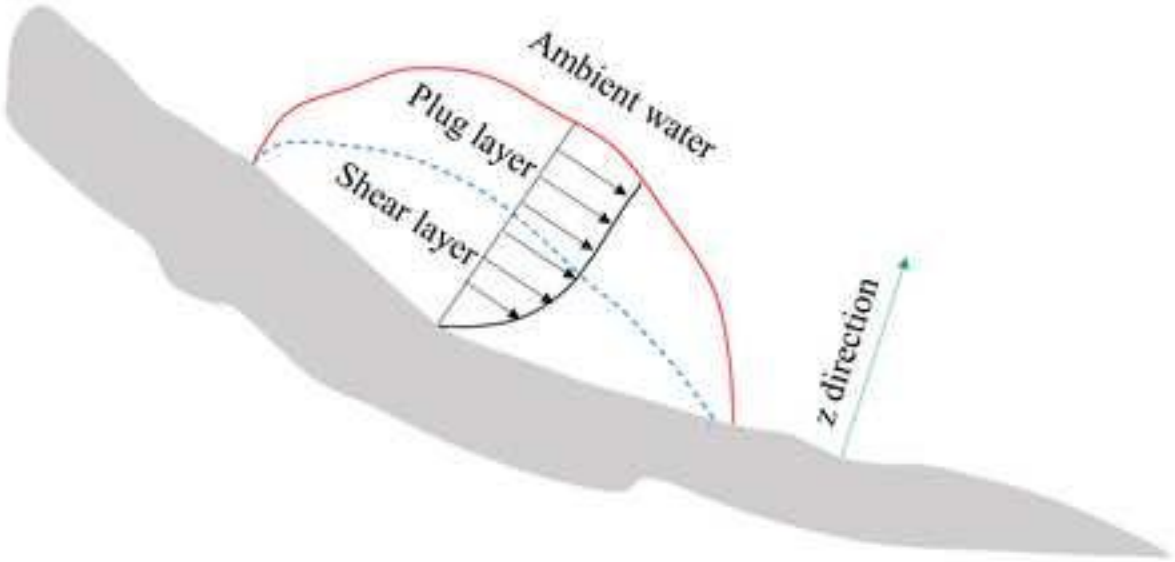

Fig. 2

Click here to download Figure Fig. 2.tif

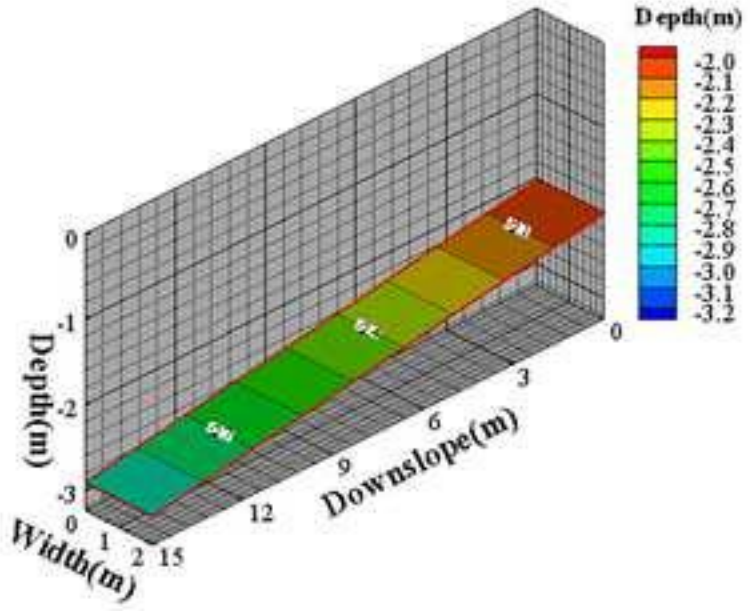

Fig. 3

Click here to download Figure Fig. 3.tif

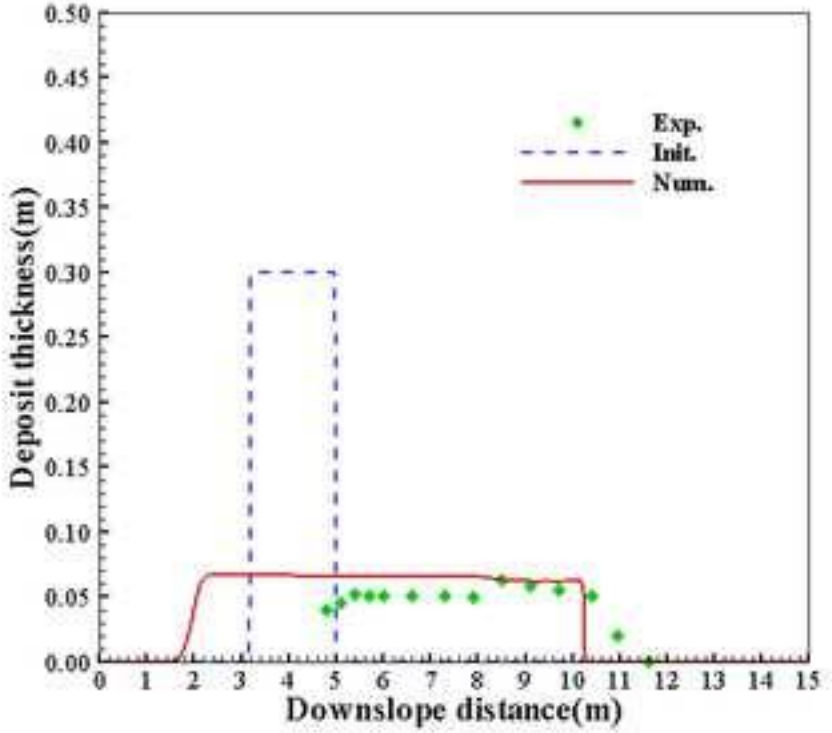

Fig. 4

Click here to download Figure Fig. 4.tif

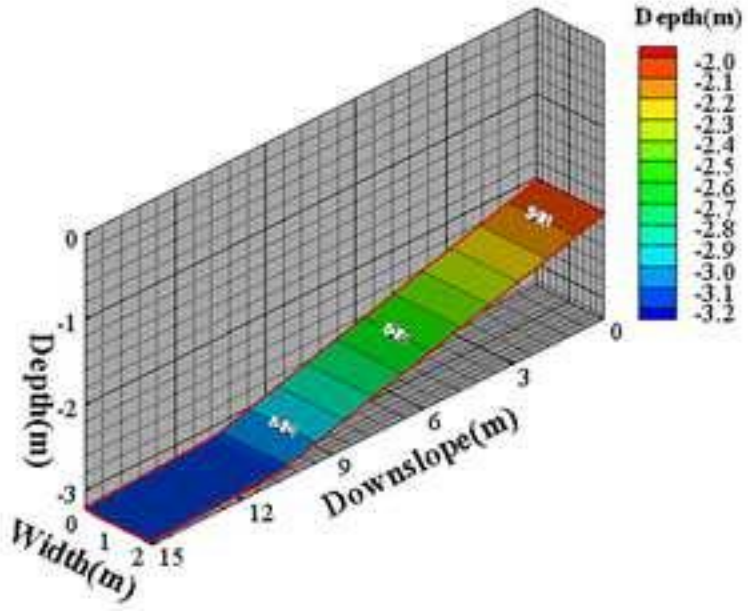

Fig. 5

Click here to download Figure Fig. 5.tif

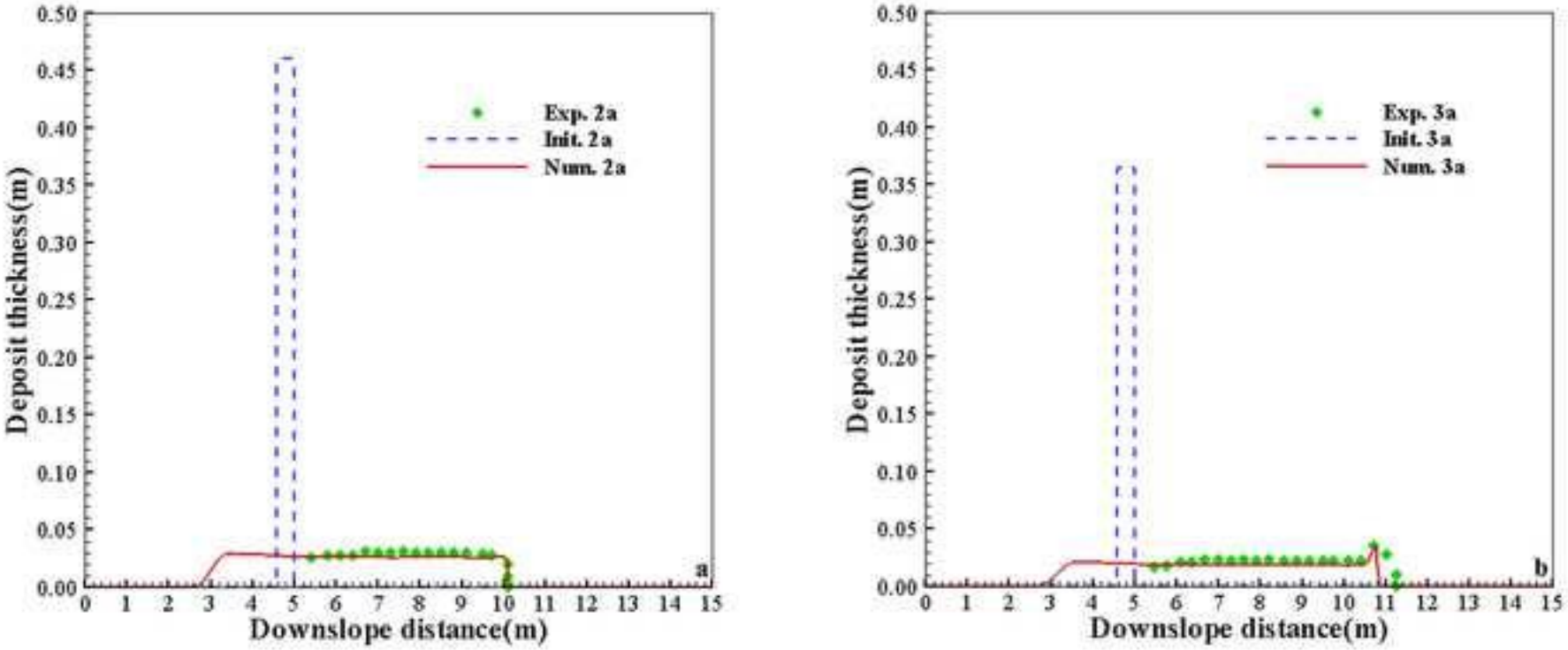

Fig. 6

Click here to download Figure Fig. 6.tif

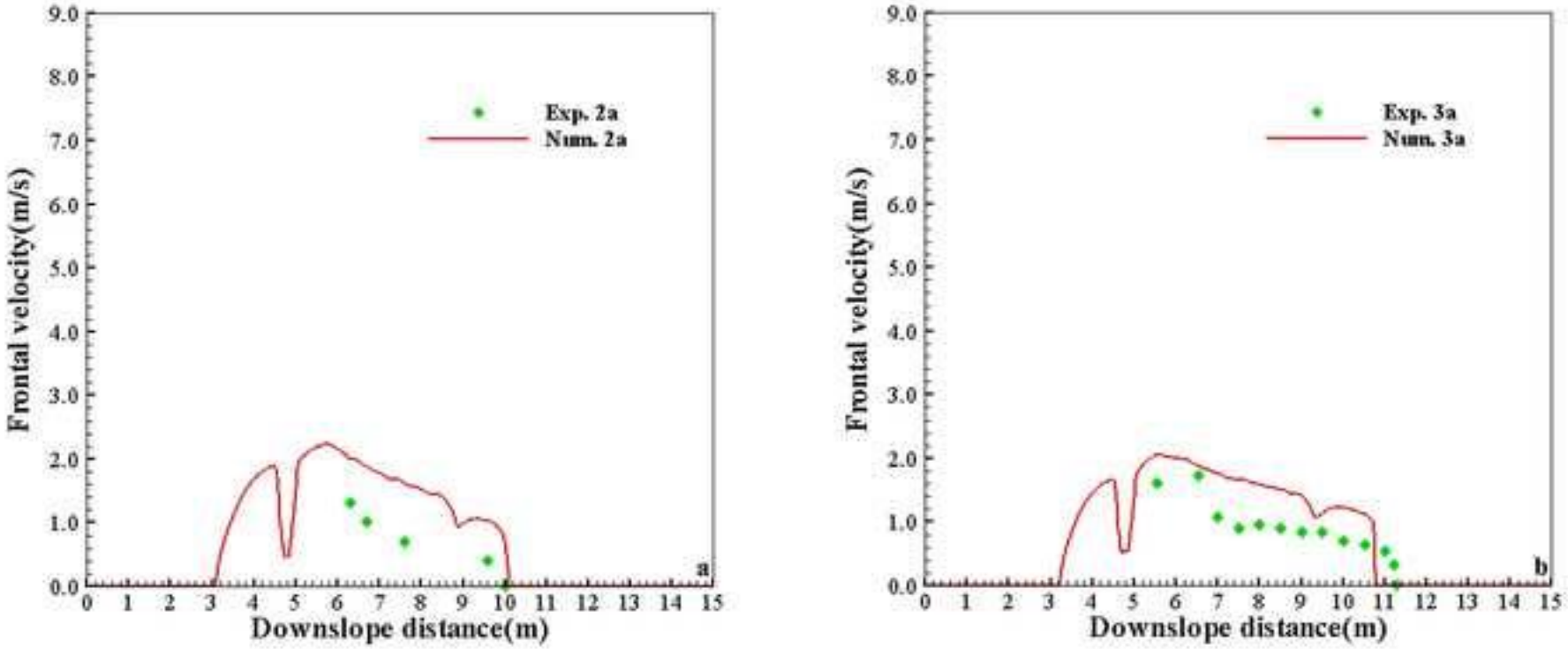

Fig. 7

Click here to download Figure Fig. 7.tif

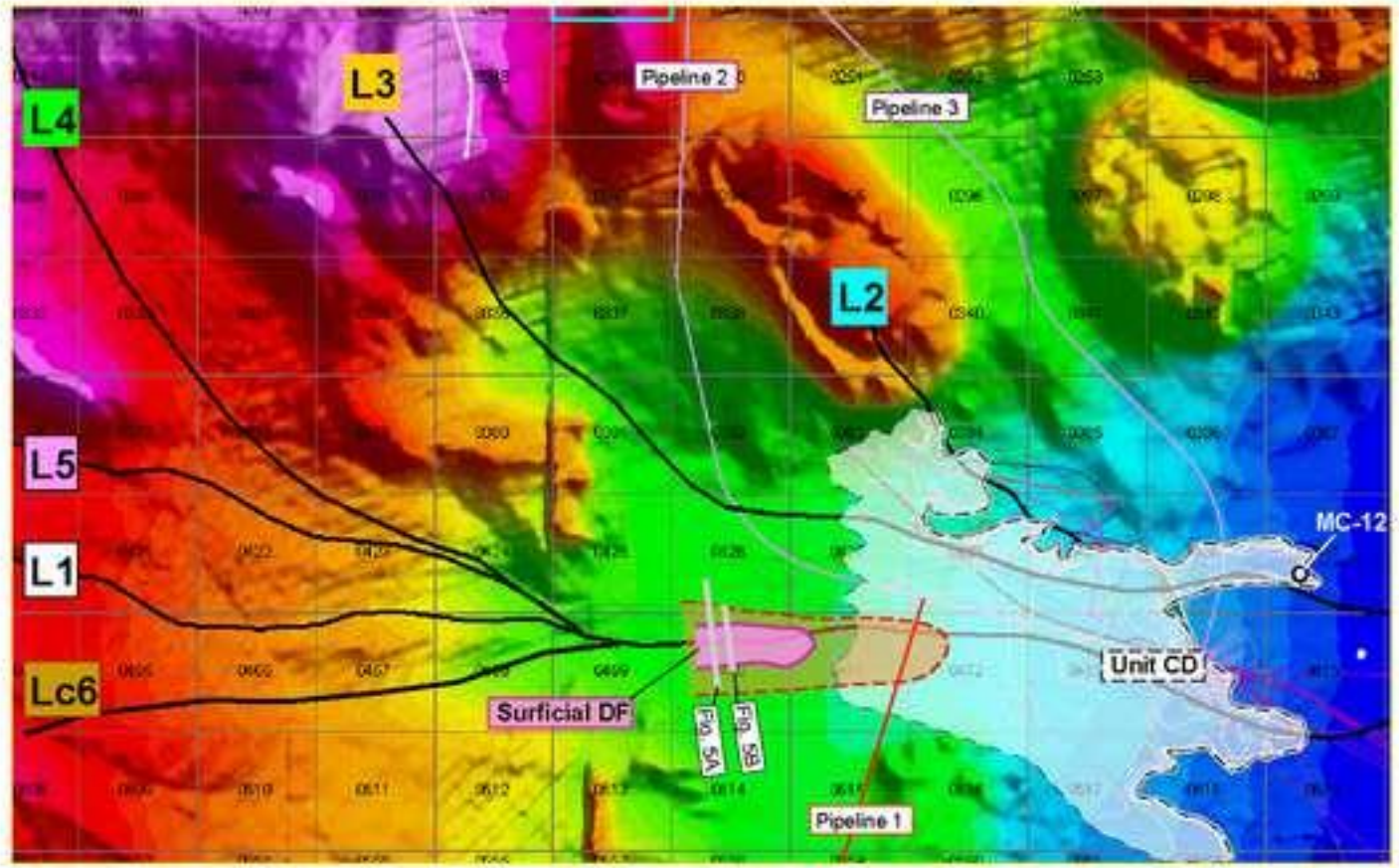

Fig. 8

Click here to download Figure Fig. 8.tif

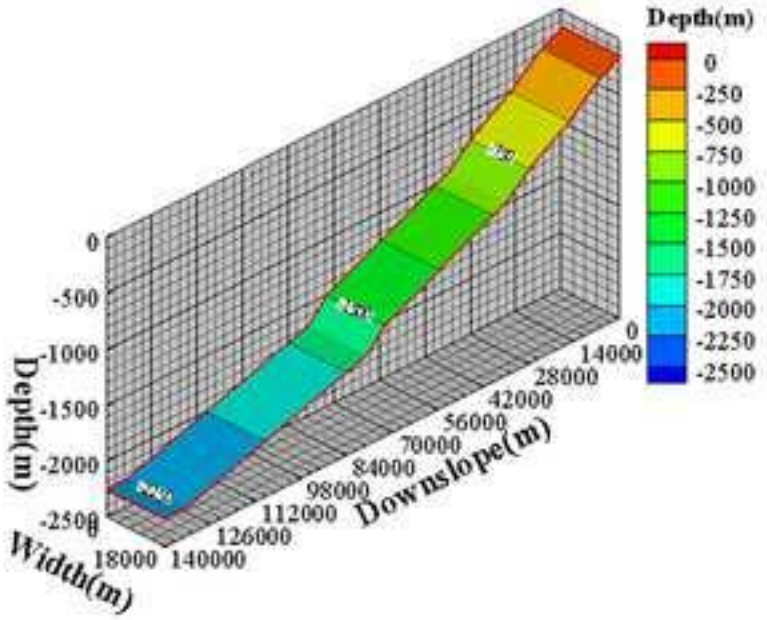

Fig. 9

Click here to download Figure Fig. 9.tif

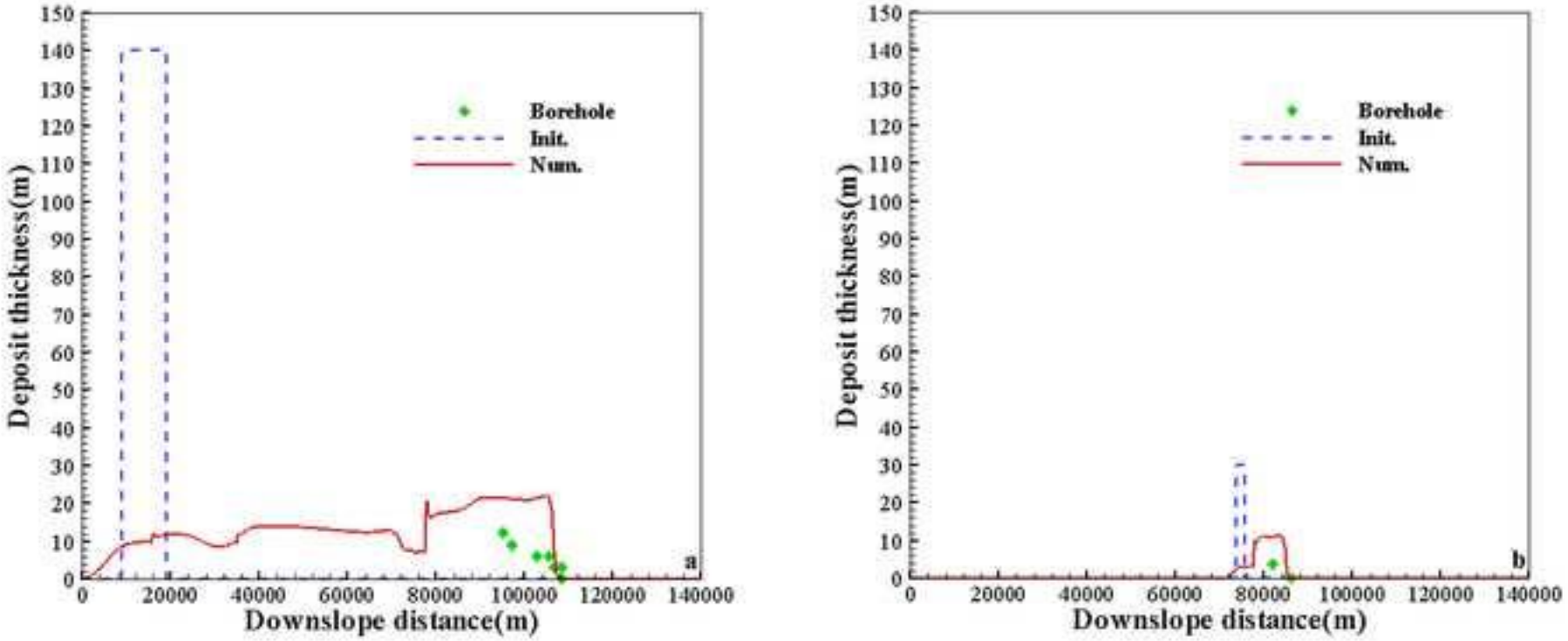

Fig. 10

Click here to download Figure Fig. 10.tif

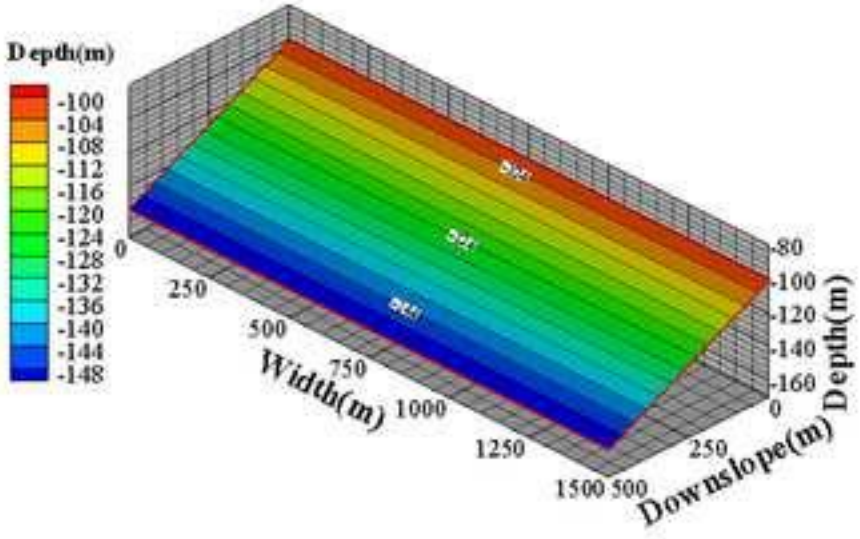

Fig. 11

Click here to download Figure Fig. 11.tif

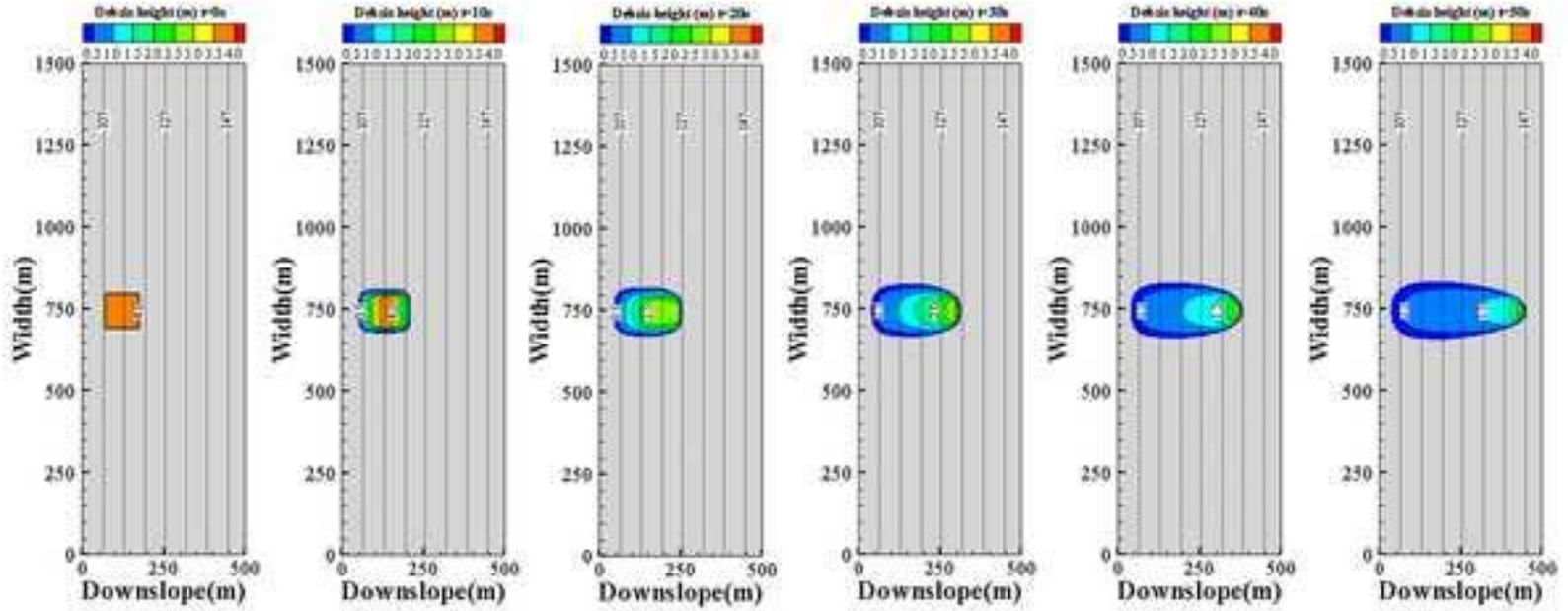

Fig. 12

Click here to download Figure Fig. 12.tif

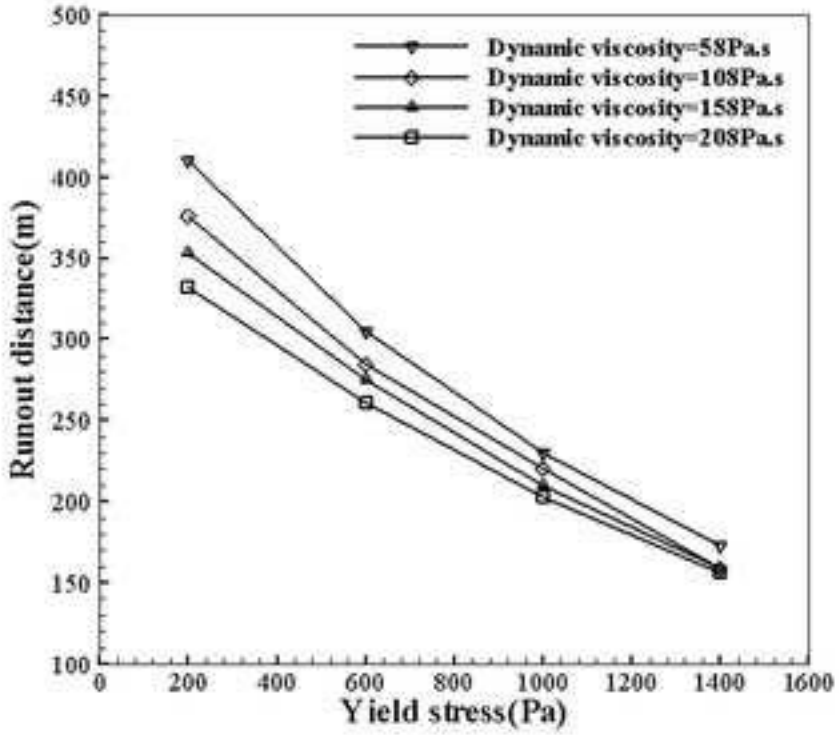

Fig. 13

Click here to download Figure Fig. 13.tif

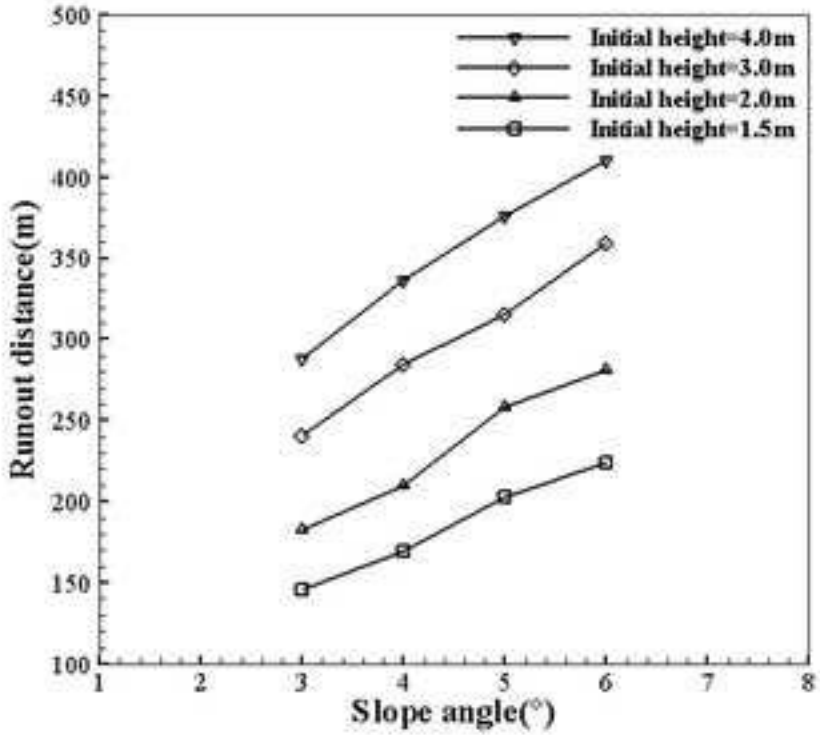

Fig. 14

Click here to download Figure Fig. 14.tif

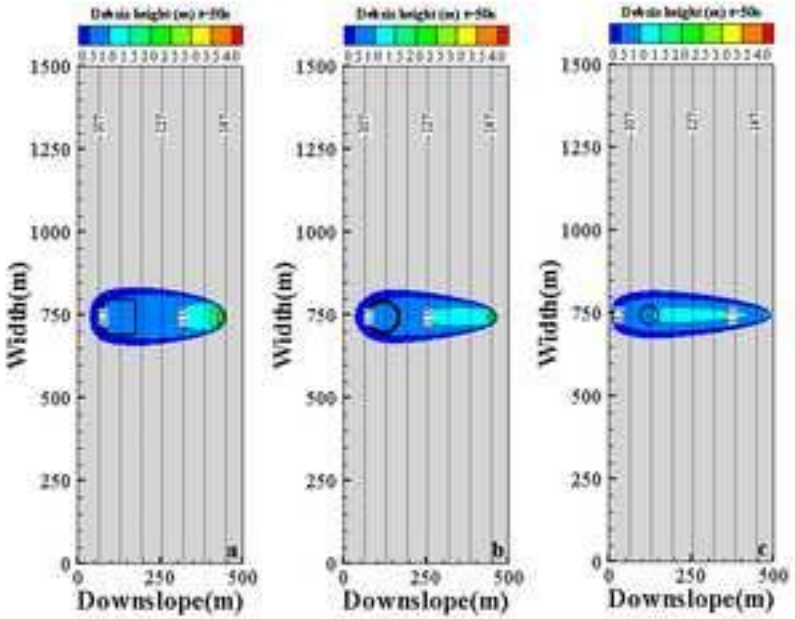

Fig. 15

Click here to download Figure Fig. 15.tif

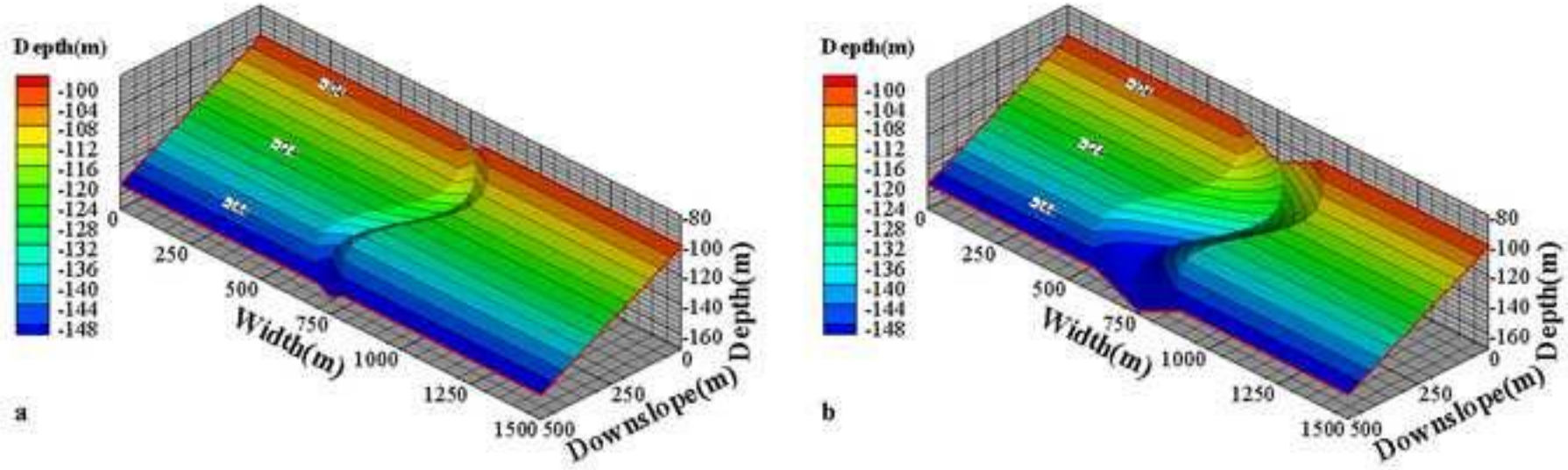

Fig. 16

Click here to download Figure Fig. 16.tif

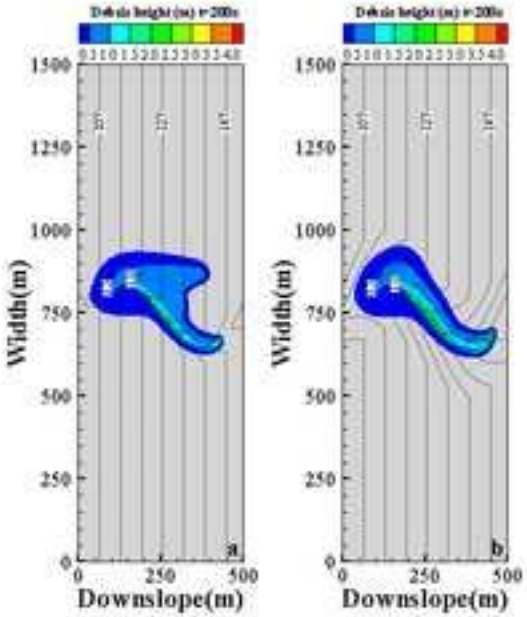

Fig. 17

Click here to download Figure Fig. 17.tif

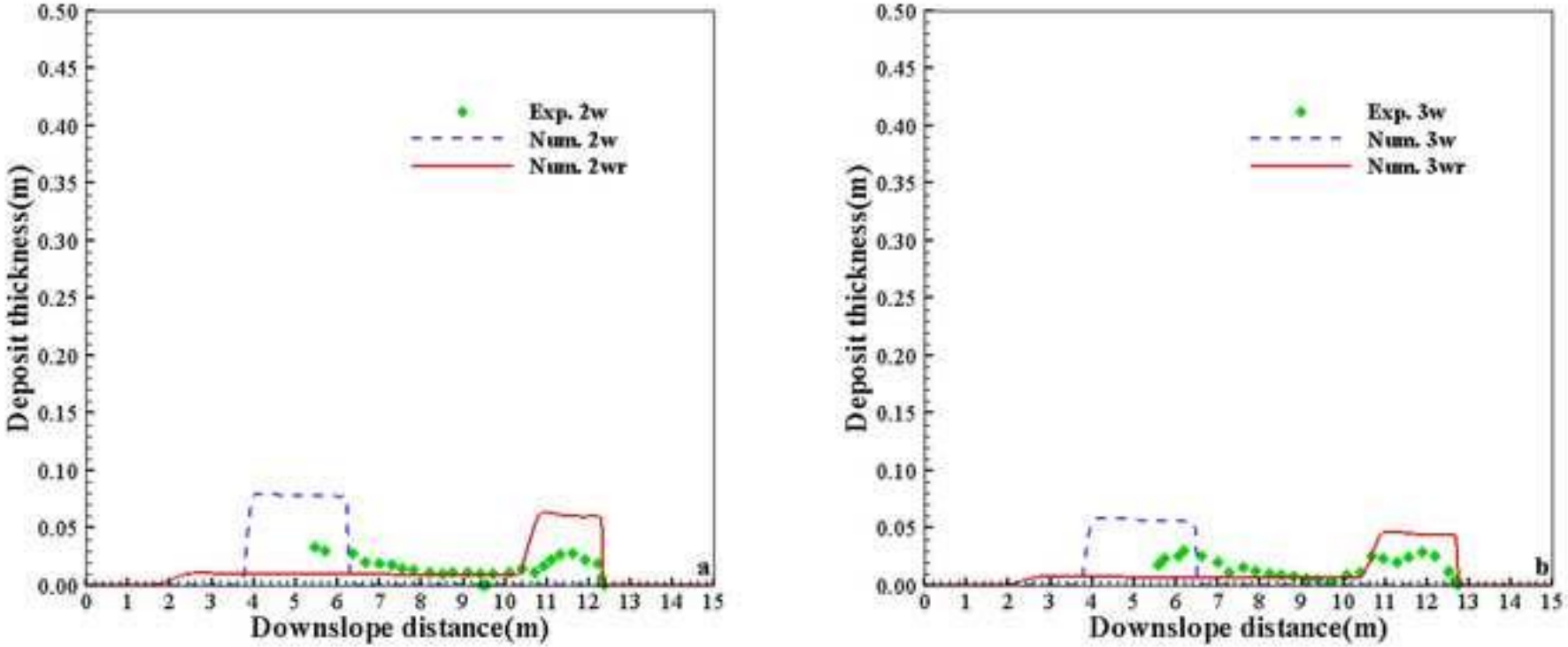

Fig. 1. Schematic of layer definition and velocity profile of submarine debris flow

Fig. 2. Channel geometry schematized from Wright and Krone (1987)

Fig. 3. Comparison between experimental and numerical results of deposit thickness (Wright and Krone 1987)

Fig. 4. Channel geometry schematized from Mohrig et al. (1999)

Fig. 5. Comparison between experimental and numerical results of deposit thickness for (a) run 2a and (b) run 3a (Mohrig et al. 1999)

Fig. 6. Comparison between experimental and numerical results of frontal velocity for (a) run 2a and (b) run 3a (Mohrig et al. 1999)

Fig. 7. Locations of surficial and buried debris flow deposits detected within the Na Kika Basin, Gulf of Mexico. Source: Pirmez et al. (2004)

Fig. 8. Bathymetry profile along L1

Fig. 9. Comparison between modelling results and borehole data of deposit thickness for (a) Unit CD and (b) Surficial DF (Pirmez et al. 2004)

Fig. 10. Schematized continental shelf with a uniform slope

Fig. 11. Deposition patterns at time interval of 10 s running for a total time of 50 s